

See discussions, stats, and author profiles for this publication at: <https://www.researchgate.net/publication/222112349>

Molecular dynamics of the primary photochemical event in rhodopsin

ARTICLE *in* JOURNAL OF THE AMERICAN CHEMICAL SOCIETY · FEBRUARY 1992

Impact Factor: 12.11 · DOI: 10.1021/ja00031a007

CITATIONS

61

READS

15

5 AUTHORS, INCLUDING:



[Leonore Findsen](#)

Purdue University

13 PUBLICATIONS 400 CITATIONS

SEE PROFILE



[Geoffrey Charles Fox](#)

Indiana University Bloomington

1,098 PUBLICATIONS 16,303 CITATIONS

SEE PROFILE



[Robert R. Birge](#)

University of Connecticut

333 PUBLICATIONS 8,994 CITATIONS

SEE PROFILE

Molecular dynamics of the primary photochemical event in rhodopsin

Jack R. Tallent, Elaine W. Hyde, Leonore A. Findsen, Geoffrey C. Fox, and Robert R. Birge

J. Am. Chem. Soc., **1992**, 114 (5), 1581-1592 • DOI: 10.1021/ja00031a007

Downloaded from <http://pubs.acs.org> on January 17, 2009

More About This Article

The permalink <http://dx.doi.org/10.1021/ja00031a007> provides access to:

- Links to articles and content related to this article
- Copyright permission to reproduce figures and/or text from this article



ACS Publications
High quality. High impact.

regression from all 11 entries in the table

$$^3J_{\text{HH}}(\theta_1, \theta_2, \phi) = 17.5 a(\theta_1, \theta_2) \cos^2 \phi + [-1949 b(\theta_1, \theta_2) - 883.3 b_2(\theta_1, \theta_2) - 1302 b_3(\theta_1, \theta_2)] \cos \phi + 3.7 \text{ Hz} \quad (18)$$

where r^2 is 0.989 and the standard deviation is 0.4 Hz. Data from eq 18 and the experimental data are entered in the seventh and eighth columns, respectively. Although the number of distinct data points is only slightly larger than the number of parameters and the range of internal angles is substantially smaller here than for the ethylenic situations in Table II, the monotonic decrease of $^3J_{\text{HH}}$ with increasing internal angle is similar. No clear trends are evident in the data for butadiene and the methyl-substituted butadienes in Table IV. In these cases it is usually assumed that conformational averaging about the C-C single bond is not a factor. Variations of $^3J_{\text{HH}}$ have been attributed to a splaying of the C=C=C angles and a concomitant compression of the C=C-H angles.^{28,29} This type of analysis was extended to *all-trans*-retinal and 11-*cis*-retinal.³⁰ Unfortunately, the spread in the vicinal H-H coupling constant values in Table IV is about the same order of magnitude as the errors in the computed values so no conclusions can be drawn in this regard.

Linear regression among the data in Table IV, with complete neglect of the θ dependence leads to the expression

$$^3J_{\text{HH}}(\phi) = 2.5 \cos^2 \phi - 3.0 \cos \phi + 5.2 \text{ Hz} \quad (19)$$

Values of $^3J_{\text{HH}}$ from eq 19 are tabulated in the sixth column of Table I. The constancy of these values clearly indicates the importance of internal angle variations for this type of coupling.

Conclusions

An analytic expression for $^3J_{\text{HH}}$ is derived and presented here to describe the dependence of vicinal H-H coupling on the internal angles θ_1 and θ_2 as well as the torsion angle ϕ . Although this study has emphasized interproton coupling, the formalism is quite generally applicable to other type of vicinal coupling constants.

The dependencies on C-C internuclear distance appear in the coefficients of the trigonometric terms. With empirical criteria for these coefficients and angular data from ab initio MO and molecular mechanics optimized structures, the resulting equations describe all types of vicinal H-H coupling, e.g., coupling in ethanic (CHCH), ethylenic (CH=CH), allylic (C=CHCH), and diene (C=CHCH=C) moieties.

The accurate specification of the vicinal H-H coupling constants in the various moieties will require more experimental data in rigid, unsubstituted molecules. Nevertheless, from this study it is now clear that vicinal coupling constants are functions of both torsion angles and internal angles. In some cases the internal angle dependence is controlled by the coefficient of the $\cos^2 \phi$ term in eq 11a which drops off monotonically. An exception is coupling in ethanic fragments having dihedral angles less than 90° because of effective cancellation between the *A* and *B* terms in this range. The coefficients of $\cos^2 \phi$ and $\cos \phi$ have almost equal slopes and effectively cancel for dihedral angles less than 90°. Thus, the usual neglect of the internal angle for ethanic coupling seems to be justified for many common situations in relatively rigid multicyclic compounds. However, for dihedral angles greater than 90° the coefficients reinforce one another, thereby leading to very large variations with internal angles.

The very important role of substituents and their orientations has not been addressed in this study. Clearly, substantial changes are expected by both substituent electronic effects and substituent-induced geometry changes. Because of the balance in the *B* term between large terms of opposite sign, it seems likely that any electronic changes such as by electronegative substituents could easily lead to a substantial change in the form of the θ dependence of *B*.

Acknowledgment. Appreciation is expressed to the National Science Foundation for a Chemical Instrumentation Grant to assist in purchasing a CONVEX 220 computer.

Molecular Dynamics of the Primary Photochemical Event in Rhodopsin

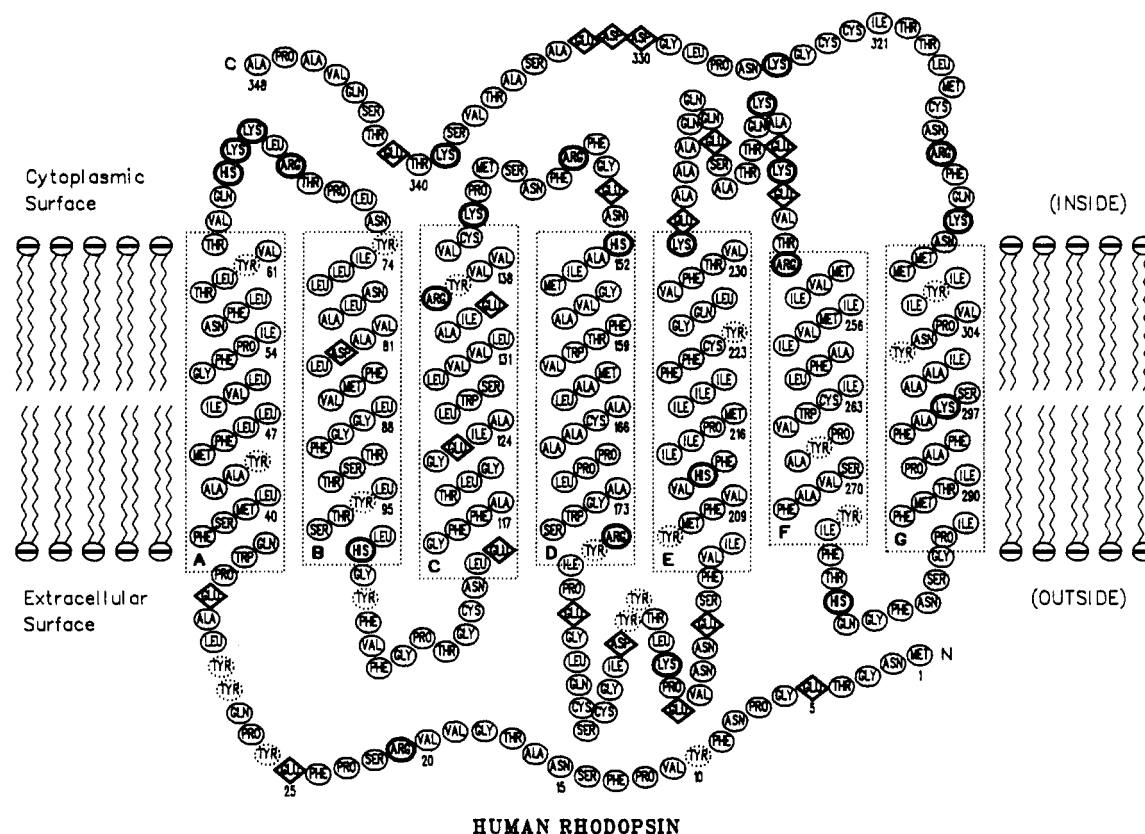
Jack R. Tallent, Elaine W. Hyde, Leonore A. Findsen, Geoffrey C. Fox, and Robert R. Birge*

Contribution from the Department of Chemistry, the Center for Molecular Electronics, and the Northeast Parallel Architecture Center, Syracuse University, Syracuse, New York 13244-4100. Received August 2, 1991

Abstract: The ground-state and excited-state surfaces connecting rhodopsin (R) and bathorhodopsin (B) along the $\phi_{11,12}$ dihedral reaction path were partially adiabatically mapped on the basis of a revised model of the protein binding site with a glutamic acid counterion interacting with the C₁₃-C₁₅ region of the chromophore. The ground-state surface was generated by using MNDO/AM1 procedures, and the excited-state surface was generated by using INDO-PSDCI procedures including both single- and double-configuration interaction. The first excited singlet state exhibits a barrierless reaction path for C₁₁=C₁₂ dihedral torsion with a local minimum (activated complex) centered at $\phi_{11,12} = 90^\circ$. Semiempirical molecular dynamics procedures are used to simulate the forward and reverse photochemistry. The activated complex is reached in ~375 fs following excitation. The quantum yields (Φ) and the product formation times (t) are calculated on the basis of three semiclassical coupling models. Best results are obtained by including both dynamic and phased (partitioned) nonadiabatic coupling (experimental values): $\Phi_{\text{R} \rightarrow \text{B}} = 0.698$ (0.67); $t_{\text{R} \rightarrow \text{B}} = 1.360$ (~3) ps; $\Phi_{\text{B} \rightarrow \text{R}} = 0.521$ (0.53); $t_{\text{B} \rightarrow \text{R}} = 1.628$ (~3) ps. The nonadiabatic coupling term changes sign at $\phi_{11,12} \cong 92^\circ$ and preferentially enhances $\Phi_{\text{R} \rightarrow \text{B}}$ relative to $\Phi_{\text{B} \rightarrow \text{R}}$. The lower quantum yield of the B → R photoisomerization is also due to the rapid arrival of the trajectory into the activated complex which precludes equilibration of the excited state prior to arrival at the activated complex and lowers the dynamic coupling term. The $S_n \leftarrow S_1$ excited singlet state spectrum is calculated as a function of time following excitation of R. The key feature of the early time spectra (0-325 fs) is the presence of a strong absorption centered between 540 and 580 nm, which is surprisingly similar in oscillator strength and energy to the λ_{max} absorption band of bathorhodopsin. This feature broadens and decreases in intensity once the molecule enters the activated complex. A longer wavelength band at ~780 nm appears after ~375 fs which is diagnostic of C₁₁=C₁₂ dihedral angles in the region $80^\circ < \phi_{11,12} < 100^\circ$. A strong $S_n \leftarrow S_1$ absorption band is calculated at ~340 nm, which is relatively insensitive in both location and intensity to changes in the C₁₁=C₁₂ dihedral angle.

Rhodopsin (MW \cong 40 000) is the protein responsible for generating an optic nerve impulse in the visual receptors of the

three phyla that possess image-resolving eyes: mollusks, arthropods, and vertebrates.^{1,2} The primary sequence^{3,4} and presumed



HUMAN RHODOPSIN

Figure 1. Amino acid sequence^{3,4} and putative membrane spanning regions¹ of human rhodopsin. Amino acid abbreviations are as follows: alanine, Ala; arginine, Arg; asparagine, Asn; aspartic acid, Asp; cysteine, Cys; glutamine, Gln; glycine, Gly; histidine, His; isoleucine, Ile; leucine, Leu; lysine, Lys; methionine, Met; phenylalanine, Phe; proline, Pro; serine, Ser; threonine, Thr; tryptophan, Trp; tyrosine, Tyr; valine, Val. Amino acids which under nominal conditions carry a charge are shown in thickened circles (positively charged) or boxes (negatively charged). The chromophore is covalently linked to the protein via a protonated Schiff linkage to Lys₂₉₆.

transmembrane assignments¹ for human rhodopsin are shown in Figure 1. Despite what is believed to be independent evolutionary development, these three phyla have converged on a remarkably similar protein structure and an identical light absorbing chromophore, 11-*cis*-retinal. At ambient temperature and neutral pH, rhodopsin undergoes a photobleaching sequence that initiates a complex series of reactions which ultimately hyperpolarize the plasma membrane of the rod cell in the retina.^{5,6} The plasma membrane contains numerous cation-specific channels which are open to sodium ion flow in the dark. Light sets off a series of biochemical reactions that block these channels, and the resultant hyperpolarization generates a more negative potential inside the cell. The key feature of this event is that a single photon of light can generate a hyperpolarization of close to 1 mV ($\sim 10^6$ Na⁺ ions blocked), which is sufficient to activate a nerve impulse in a dark-adapted retina.

The primary photochemical even in rhodopsin involves an 11-*cis* to 11-*trans* photoisomerization of the protein-bound retinyl chromophore.¹ This conformational change involves rearrangement of a large fraction of the retinyl polyene and stores ~ 32 kcal mol⁻¹ of energy.⁷⁻⁹ The observation that bathorhodopsin forms in a few picoseconds^{10,11} with a temperature-independent

quantum yield of 0.67¹²⁻¹⁵ places rather severe constraints on the nature of the excited-state dynamics. Approximately 10 years ago, Birge and Hubbard carried out molecular dynamics calculations on the primary event and predicted a bathorhodopsin formation time of 2.3 ps with a quantum yield of 0.61.¹⁶⁻¹⁸ More recent experimental studies indicate that the binding site model adopted by Birge and Hubbard is incorrect (for a review, see ref 1). Not only did the original model underestimate energy storage, the binding site model placed the counterion too close to the imine end of the retinyl polyene. Furthermore, the molecular dynamics calculations ignored nonadiabatic coupling in the quantum yield calculations. In contrast, Weiss and Warshel have concluded that nonadiabatic coupling is the dominant mode of coupling into the ground state.¹⁹

The above considerations prompted our reevaluation of the potential surfaces and molecular dynamics of the primary event in rhodopsin. The key goals of the present study are to provide a more accurate model of the photochemical transformation, the ground- and excited-state potential surfaces, and the photophysical

- (1) Birge, R. R. *Biochim. Biophys. Acta* **1990**, *1016*, 293-327.
- (2) Birge, R. R. *Annu. Rev. Phys. Chem.* **1990**, *41*, 683-733.
- (3) Nathans, J.; Hogness, D. S. *Proc. Natl. Acad. Sci. U.S.A.* **1984**, *81*, 4851-4855.
- (4) Nathans, J.; Hogness, D. S. *Cell* **1983**, *34*, 807-814.
- (5) Stryer, L. *Annu. Rev. Neurosci.* **1986**, *9*, 87-119.
- (6) Liebman, P. A.; Parker, K. R.; Dratz, E. A. *Annu. Rev. Physiol.* **1987**, *49*, 965-991.
- (7) Cooper, A. *FEBS Lett.* **1979**, *100*, 382-384.
- (8) Cooper, A. *Nature (London)* **1979**, *282*, 531-533.
- (9) Schick, G. A.; Cooper, T. M.; Holloway, R. A.; Murray, L. P.; Birge, R. R. *Biochemistry* **1987**, *26*, 2556-2562.
- (10) Peters, K. S.; Applebury, M. L.; Rentzepis, P. M. *Proc. Natl. Acad. Sci. U.S.A.* **1977**, *74*, 3119-3123.

- (11) Monger, T.; Alfano, R. R.; Callender, R. H. *Biophys. J.* **1979**, *27*, 105-115.
- (12) Dartnall, H. J. A. In *Handbook of sensory physiology*; Dartnall, H. J. A., Ed.; Springer-Verlag, Heidelberg: 1972; pp 122-145.
- (13) Hurley, J. B.; Ebrey, T. G.; Honig, B.; Ottolenghi, M. *Nature (London)* **1977**, *270*, 540-542. Rosenfeld, T.; Honig, B.; Ottolenghi, M.; Hurley, J. B.; Ebrey, T. G. *Pure Appl. Chem.* **1977**, *49*, 341-351.
- (14) Suzuki, T.; Callender, R. H. *Biophys. J.* **1981**, *34*, 261-265.
- (15) Birge, R. R.; Callender, R. H. In *Biophysical studies of retinal proteins*; Ebrey, T.; Frauenfelder, H.; Honig, B.; Nakanishi, K., Eds.; University of Illinois Press: Champaign, 1987; pp 270-281.
- (16) Birge, R. R. In *Biological events probed by ultrafast laser spectroscopy*; Alfano, R. R., Ed.; Academic Press: New York, 1982; pp 299-317.
- (17) Birge, R. R.; Hubbard, L. M. *Biophys. J.* **1981**, *34*, 517-534.
- (18) Birge, R. R.; Hubbard, L. M. *J. Am. Chem. Soc.* **1980**, *102*, 2195-2204.
- (19) Weiss, R. M.; Warshel, A. *J. Am. Chem. Soc.* **1979**, *101*, 6131-6133.

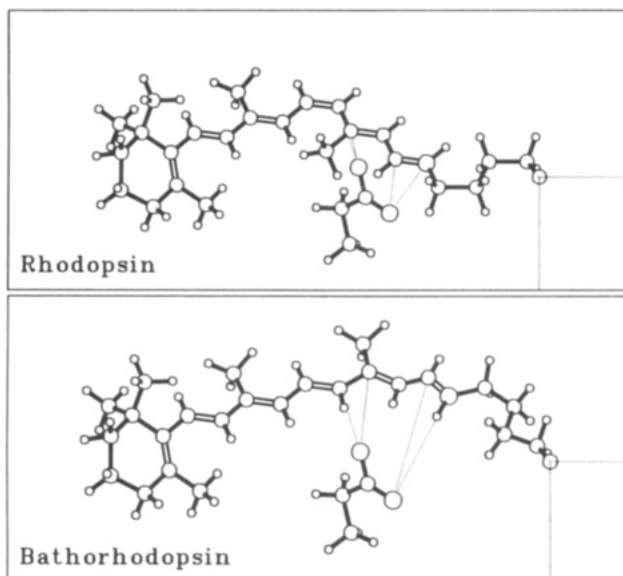


Figure 2. Our model of the binding site of rhodopsin (top) and the primary photochemical event that generates bathorhodopsin (bottom) based on the available spectroscopic, photocalorimetric, and quantum efficiency data.²⁰ Key chromophore-counterion electrostatic interactions are indicated with dashed lines. The counterion is represented in the calculations by using a fixed $\text{CH}_2\text{CH}_2\text{CO}_2^-$ moiety to represent a glutamic acid residue on helix C.^{21,22} The position of the counterion was optimized to reproduce as closely as possible the absorption maxima of rhodopsin and bathorhodopsin as well as the energy storage in bathorhodopsin.⁹ Note that the binding site is neutral.²³

origins of the forward and reverse quantum yields based on both dynamic and nonadiabatic coupling into the ground state. In addition, we have carried out simulations of the excited-state absorption spectra which should be useful to experimentalists carrying out time-resolved spectroscopic studies of the primary event.

Results and Discussion

This study is based on the revised rhodopsin (Rho) \rightarrow bathorhodopsin (Batho) binding site models shown in Figure 2. The experimental and theoretical rationale behind the revised models has been discussed in detail previously,²⁰ and reconciliation with the various literature models is discussed in a recent review.¹ The following section provides a selective discussion on some of the key issues associated with the revised binding site model. The subsequent section discusses the use of these models to generate the ground- and excited-state potential energy surfaces. It should be noted at the outset, however, that the models shown in Figure 2 were optimized to best fit a wide variety of experimental data including vibrational and electronic spectra, quantum efficiency data, and energy storage in bathorhodopsin.²⁰ Thus, optimization of the binding site geometries required repeated generation of the ground-state and Franck-Condon excited-state potential surfaces to test the validity of the models. Thus, independent discussion should not be interpreted to suggest that the potential surfaces were generated as an exercise independent of binding site optimization.

Rhodopsin and Bathorhodopsin Binding Sites Models. Spectroscopic and neutron diffraction studies, amino acid composition, and analogies with bacteriorhodopsin suggest the secondary structure shown in Figure 1.^{1,3,4,24-27} Thus, rhodopsin spans the

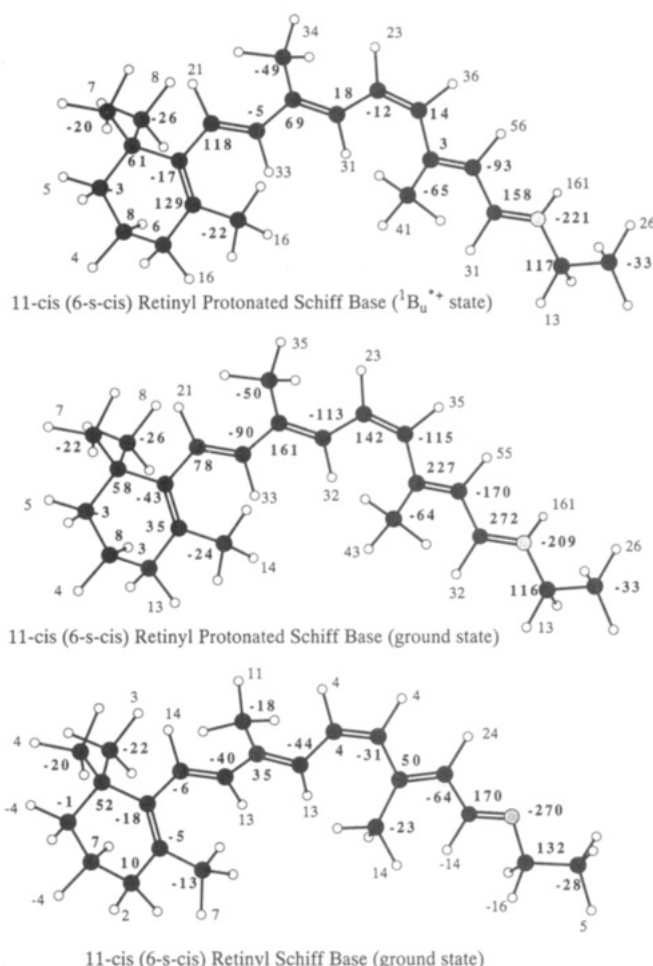


Figure 3. Atomic charge distributions in the ground state of the Schiff base and the ground and lowest excited singlet states of the protonated Schiff base of the 11-cis,6-s-cis-retinyl polyene. The charges are in electron units $\times 1000$, and the carbon and nitrogen atom charges are in boldface. The hydrogen atom charges for aliphatic environments are averaged, and the averaged charge is listed by only one atom. The calculations were carried out by holding the 6-s-cis linkage at a dihedral angle of 50° and minimizing the geometry by using MNDO/2-AM1 procedures. The resulting coordinates were then used in an INDO-PSDCI calculation including the lowest 200 single and the lowest 400 double excitations in the CI manifold. The geometries shown are not the optimized geometries but were generated artificially to enhance viewing of all of the atoms.

membrane seven times, and it is likely that the 11-cis chromophore linked to Lys₂₉₆ spans an interhelix region similar to that in bacteriorhodopsin. Two-photon studies indicate that the binding site is neutral,^{23,28,29} and hence there is only one negatively charged counterion in the vicinity of the chromophore. Based on the proposed secondary structure, there are four amino acids that are realistic candidates for the single primary counterion: Asp₈₃ (B helix), Glu₁₁₃ (C helix), Glu₁₂₂ (C helix), and Glu₁₃₄ (C helix). However, if the structure of the interhelical region surrounding the chromophore is at all similar to that of bacteriorhodopsin, it

(20) Birge, R. R.; Einterz, C. M.; Knapp, H. M.; Murray, L. P. *Biophys. J.* **1988**, *53*, 367-385.

(21) Zhukovsky, E. A.; Oprian, D. D. *Science* **1989**, *246*, 928-930.

(22) Sakmar, T. P.; Franke, R. R.; Khorana, H. G. *Proc. Natl. Acad. Sci. U.S.A.* **1989**, *86*, 8309-8313.

(23) Birge, R. R.; Murray, L. P.; Pierce, B. M.; Akita, H.; Balogh-Nair, V.; Findsen, L. A.; Nakanishi, K. *Proc. Natl. Acad. Sci. U.S.A.* **1985**, *82*, 4117-4121.

(24) Hargrave, P. A. *Prog. Retinal Res.* **1982**, *1*, 1-51.

(25) Hargrave, P. A.; McDowell, J. H.; Curtis, D. R.; Wang, J. K.; Juszczak, E.; Fong, S. L.; Rao, J. K. M.; Argos, R. *Biophys. Struct. Mech.* **1983**, *9*, 235-244.

(26) Hargrave, P. A.; McDowell, J. H.; Feldman, R. J.; Atkinson, P. H.; Mohana Rao, J. K.; Argos, P. *Vision Res.* **1984**, *24*, 1487-1499.

(27) Adams, G.; McDowell, J. H.; Arendt, A.; Hargrave, P. A.; Smyk-Randall, E.; Sheehan, J. In *Biophysical studies of retinal proteins*; Ebrey, T. G., Frauenfelder, B., Honig, K., Nakanishi, K., Eds.; University of Illinois Press: Champaign, 1987; pp 86-94.

(28) Birge, R. R. *Acc. Chem. Res.* **1986**, *19*, 138-146.

(29) Murray, L. P.; Findsen, L. A.; Pierce, B. M.; Birge, R. R. In *Fluorescence in the biomedical sciences*; Taylor, D. L., Waggoner, A., Lannie, R., Murphy, R., Birge, R. R., Eds.; Liss: New York, 1986; pp 105-127.

is highly unlikely that the counterion could be attached to helix B. We know from one-photon²⁰ and two-photon²³ spectroscopic studies that the key perturbations involve C₁₃-CTN and C₁₅-CTN chromophore-counterion (CTN) interactions. This observation suggests that the counterion is likely attached to either helix C or F. Although there are two tyrosine residues on helix F, the spectroscopic properties of rhodopsin are not consistent with a tyrosinate primary counterion.²⁰ Recent site-directed mutagenesis studies suggest that Glu₁₁₃ is the primary counterion,^{21,22} but these studies could also be interpreted to indicate that Glu₁₁₃ is essential in forming the chromophore binding site but that another counterion is interacting with the chromophore. It is likely, however, that the primary counterion is one of the glutamic acid residues on helix C. A model of the rhodopsin binding site that is consistent with the available spectroscopic and chemical data is shown in Figure 2. Models which move the counterion one or two atoms closer to the center of the polyene chain and simultaneously closer to the polyene atoms are also possible. However, the positive charge is primarily localized on atoms C₁₃, C₁₅, and the imine proton (see Figure 3), and one oxygen atom must be within ~4 Å of this section to accommodate the transition energy and oscillator strength data.²⁰

Many literature models, including the binding site model adopted in our previous molecular dynamics studies of rhodopsin,¹⁶⁻¹⁸ provide for electrostatic interaction between the counterion and the imine proton. A strong proton-counterion interaction has often been implicated in the observation of the large ND shift of 33 cm⁻¹. However, as noted by Birge,¹ water within the binding site may be responsible. One or more water molecules are known to be present within the rhodopsin binding site.³⁰ It is generally recognized that a large $\nu_{C=N}$ deuterium (ND shift) isotope shift is characteristic of strong hydrogen bonding to the imine proton.³¹⁻³³ On the basis of this argument, hydrogen bonding is strongest in rhodopsin (ND shift ~33 cm⁻¹), strong in bathorhodopsin (ND shift ~31 cm⁻¹), and moderately strong in isorhodopsin (ND shift ~24 cm⁻¹). As comparison, the all-trans protonated Schiff base (ATPSB) in methanol exhibits a ND shift of ~26 cm⁻¹. Spectroscopic studies of ATPSB indicate that the counterion is intimately associated with the imine proton in nonpolar environments.³⁴ The work of Blatz³⁵ suggests that in highly polar, strongly hydrogen bonding solvents the counterion is highly solvated and the imine proton is hydrogen bonded with the solvent. The ND shift has been measured for ATPSB in both environments and differs by only 3 cm⁻¹.^{31,32,36} One concludes that the ND shift, while diagnostic of hydrogen bonding, is not sensitive to the nature of the hydrogen bond. A quantitative relationship between the ND shift and the strength of a hydrogen bond to the imine proton has not been firmly established (for more details see refs 32 and 37-39). Although the ND shift is largest in rhodopsin, it drops by only 2 cm⁻¹ in going from rhodopsin to bathorhodopsin. This difference is anomalously small for an isomerization moving the C₁₅=NH moiety away from a fixed counterion. Any attempt to maintain a strong hydrogen bond between the imine proton and the counterion following a one-bond

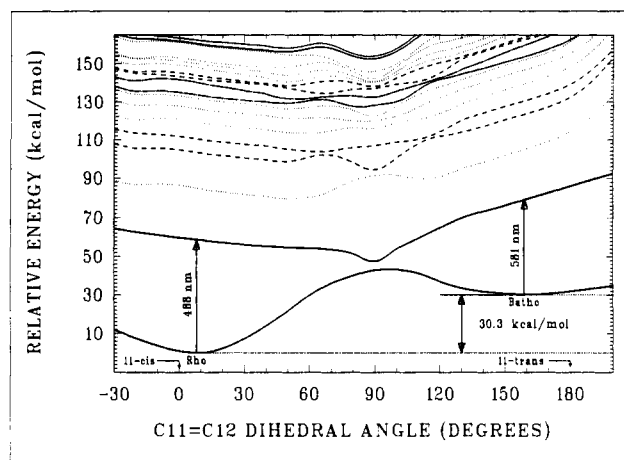


Figure 4. Ground and lowest 17 excited singlet state potential surfaces as a function of the C₁₁=C₁₂ dihedral angle. The ground-state and lowest excited singlet state surfaces are adiabatically mapped as a function of all degrees of freedom of the chromophore (see Figure 2) with the exception of the $\phi_{11=12}$ (ordinate) and the β -ionylidene ring, which was held fixed. The excited singlet state surfaces are calculated as a function of the first excited singlet state geometry to facilitate the calculation of $S_n \leftarrow S_1$ spectra. Those excited singlet states that are calculated to have $S_n \leftarrow S_1$ oscillator strengths less than 0.1 for all C₁₁=C₁₂ dihedral angles are shown with dotted lines (---). Those excited singlet states that are calculated to have $S_n \leftarrow S_1$ oscillator strengths greater than 0.1 for all C₁₁=C₁₂ dihedral angles are shown with dashed (---) lines. The 8th and 9th excited singlet states are calculated to have $S_n \leftarrow S_1$ oscillator strengths greater than 0.1 for C₁₁=C₁₂ dihedral angles less than 90° and greater than 0.1 for C₁₁=C₁₂ dihedral angles greater than 90° are shown with dashed-dotted (-.-.-) lines. The 16th excited singlet state is shown with a solid line and is calculated to have a negligible $S_{16} \leftarrow S_1$ oscillator strength in all regions except for $\phi_{11=12}$ near 90°. (The 17th excited singlet state has a negligible oscillator strength.)

11-cis \rightarrow 11-trans photoisomerization will fail to accommodate the observed oscillator strength and spectral shifts.

The remarkable similarity of $\nu_{C=NH}$ and $\nu_{C=ND}$ in rhodopsin, bathorhodopsin, and isorhodopsin argues against those binding site models that propose hydrogen bonding between the counterion and the imine proton in rhodopsin and isorhodopsin and an uncharged protein residue in bathorhodopsin. The force field calculations of Deng and Callender³² and the model compound studies of Baasov et al.⁴⁰⁻⁴² indicate that $\nu_{C=NH}$ and $\nu_{C=ND}$ are sensitive to the charge on the hydrogen bonding species. For reasons discussed in detail in refs 1 and 20, we conclude that hydrogen bonding of the imine proton to water provides the best model, because it explains both the magnitude and the similarity in the ND shift observed in rhodopsin, bathorhodopsin, and isorhodopsin.

We have not included water in our molecular dynamics simulations, however, for two reasons. First, it is not clear whether the water molecule associated with the imine proton remains associated with the proton during isomerization or is kinetically stripped from the chromophore during the photoisomerization. (If kinetic stripping of water occurs, however, the observations noted in the previous paragraph suggest that a water molecule is associated with the imine proton in "relaxed" bathorhodopsin.) Second, and more practical, the additional computational effort precluded implementation at the procedural level adopted here. Preliminary calculations indicate that there are multiple potential energy minima for the water coordinate that are very similar in energy but yield different excited-state potential surfaces. A considerable computational effort will be required to explore adequately the potential surfaces of the rhodopsin chromophore when one or more water molecules are included in the binding

(30) Rafferty, C. N.; Shichi, H. *Photochem. Photobiol.* **1981**, *33*, 229-234.

(31) Palings, J.; Pardo, J. A.; van der Berg, E.; Winkel, C.; Lugtenburg, J.; Mathies, R. S. *Biochemistry* **1987**, *26*, 2544-2556.

(32) Deng, H.; Callender, R. H. *Biochemistry* **1987**, *26*, 7418-7426.

(33) Bagley, K.; Balogh-Nair, V.; Croteau, A. A.; Dollinger, G.; Ebrey, T. G.; Eisenstein, L.; Hong, M. K.; Nakanishi, K.; Vittitow, J. *Biochemistry* **1985**, *24*, 6055-6071.

(34) Birge, R. R.; Murray, L. P.; Zidovetzki, R.; Knapp, H. M. *J. Am. Chem. Soc.* **1987**, *109*, 2090-2101.

(35) Blatz, P. E.; Mohler, J. H.; Navangul, H. V. *Biochemistry* **1972**, *11*, 848-855.

(36) Smith, S. O.; Myers, A. B.; Mathies, R. A.; Pardo, J. A.; Winkel, C.; Van Den Berg, E. M. M.; Lugtenburg, J. *Biophys. J.* **1985**, *47*, 653-664.

(37) Lopez-Garriga, J. J.; Babcock, G. T.; Harrison, J. F. *J. Am. Chem. Soc.* **1986**, *108*, 7241-7251.

(38) Lopez-Garriga, J. J.; Babcock, G. T.; Harrison, J. F. *J. Am. Chem. Soc.* **1986**, *108*, 7131-7133.

(39) Kakitani, H.; Kakitani, T.; Rodman, H.; Honig, B. *J. Phys. Chem.* **1983**, *87*, 3620-3628.

(40) Baasov, T.; Sheves, M. *Isr. J. Chem.* **1985**, *25*, 53-55.

(41) Baasov, T.; Friedman, N.; Sheves, M. *Biochemistry* **1987**, *26*, 3210-3217.

(42) Baasov, T.; Friedman, N.; Sheves, M. In *Biophysical Studies of retinal proteins*; Ebrey, T. G., Frauenfelder, H., Honig, B., Nakanishi, K., Eds.; University of Illinois Press: Champaign, 1987; pp 252-261.

site. These studies are currently in progress, but it is apparent that these studies will require the use of revised molecular orbital procedures capable of treating hydrogen bonding at a level more sophisticated than is inherent in the semiempirical models employed in the present study.

Generating the model for the primary event and the resulting bathorhodopsin geometry was accomplished by modifying the chromophore-counterion interaction (within the constraints discussed above) and the lysine geometry to provide the best possible fit to three experimental parameters: the absorption maxima of rhodopsin ($\lambda_{\text{max}} = 498$ nm) and bathorhodopsin ($\lambda_{\text{max}} = 535$ nm) and the energy storage in bathorhodopsin (32 kcal mol⁻¹).⁹ We discuss the details in the next section.

Potential Energy Surfaces. Ground and first excited singlet state potential energy surfaces were generated via partial adiabatic mapping, and the results are shown in Figure 4. The ground-state surface was calculated as a function of $\phi_{11,12}$ by using MNDO/AM1 molecular orbital procedures^{43,44} to minimize all of the degrees of freedom of the chromophore with the exception of the β -ionylidene ring and the α and β carbon atoms of the lysine residue. The entire counterion was also fixed in space after its location was optimized as described in the previous section. The above geometric constraints are appropriate for a protein binding site that has covalent linkages of the lysine residue and the counterion to the transmembrane α -helical segments and a β -ionylidene binding site that is constrained on the <3-ps time scale of the primary event.

The excited-state surface was partially adiabatically mapped by using the following protocol. First, a Franck-Condon surface as a function of $\phi_{11,12}$ was generated by using the ground-state adiabatic geometry and INDO-PSDCI molecular orbital procedures^{17,18,45} with the lowest energy 200 single and lowest energy 400 double excitations included in the configuration interaction calculation. Next, the potential well associated with the activated complex ($80^\circ \leq \phi_{11,12} \leq 100^\circ$) was adiabatically minimized in 2.5° increments subject to the same geometric constraints that were used in the generation of the ground-state surface (see above). The excited-state surface in the regions ($0^\circ \leq \phi_{11,12} < 80^\circ$) and ($100^\circ < \phi_{11,12} \leq 160^\circ$) was similarly minimized in 5° increments. Because the excited-state calculations included single and double CI, analytical derivatives could not be calculated and it was necessary to use numerical procedures to minimize the energy. The added computational burden associated with the generation of numerical derivatives requires a significant increase in computer time to calculate the minimized geometries. The calculations were made more tractable by fixing all of the C-H bond lengths to the ground-state values.

The Franck-Condon and minimized excited-state surfaces were merged into a reaction path surface by using a weighting scheme that dynamically interpolates between the two surfaces based on the excited-state dynamics. That is, at the starting $C_{11}=C_{12}$ dihedral angles ($\phi_{11,12} = 6^\circ$ (Rho) and $\phi_{11,12} = 160^\circ$ (Batho)), the Franck-Condon state is given unity weight, whereas within the activated complex ($80^\circ \leq \phi_{11,12} \leq 100^\circ$) the adiabatic excited-state geometry is given unity weight. Intermediate regions are exponentially interpolated on the basis of trajectory calculations, and three iterations were required to reach a stable interpolated excited-state surface. The exponential least-squares fit yields

$$E_{\text{dyn}}^{\text{S}_1} = \xi(\phi)E_{\text{ad}}^{\text{S}_1} + (1 - \xi(\phi))E_{\text{FC}}^{\text{S}_1} \quad (1)$$

where $E_{\text{dyn}}^{\text{S}_1}$ is the resultant (dynamically minimized) first excited singlet state energy, $E_{\text{ad}}^{\text{S}_1}$ is the adiabatic (S_1 geometry minimized) first excited singlet state energy, $E_{\text{FC}}^{\text{S}_1}$ is the (S_0 geometry minimized) Franck-Condon first excited singlet state energy, and $\xi(\phi)$

is the least-squares fit weighting function

$$\begin{aligned} \xi(\phi) = & 0.56812 \exp(-4.33217 + 0.17329\phi - 0.0017329\phi^2) \\ & - 0.35124 \exp(-8.49105 + 0.24260\phi - 0.0017329\phi^2) \\ & + 1.75431 \exp(-11.09035 + 0.27726\phi - 0.0017329\phi^2) \\ & - 1.38520 \exp(-14.03623 + 0.31192\phi - 0.0017329\phi^2) \\ & + 1.13470 \exp(-17.32870 + 0.34657\phi - 0.0017329\phi^2) \\ & + 0.43313 \exp(-24.95330 + 0.41589\phi - 0.0017329\phi^2) \end{aligned} \quad (2)$$

where ϕ is the $C_{11}=C_{12}$ dihedral angle in degrees. Selected values of the weighting function $\xi(\phi)$ as a function of ϕ are as follows (ϕ in degrees in parentheses): $\xi(\phi) = 0.0352$ (10°), 0.1180 (20°), 0.2827 (30°), 0.4976 (40°), 0.6898 (50°), 0.8400 (60°), 1.00 ± 0.01 ($80-110^\circ$ (the activated complex)), 0.8137 (120°), 0.5382 (130°), 0.2725 (140°), 0.1036 (150°), 0.0290 (160°), 0.0059 (170°). The $E_{\text{dyn}}^{\text{S}_1}$ surface is shown in Figure 4.

We also calculated the energies and $S_n \leftarrow S_1$ oscillator strengths of the next 17 excited singlet states ($S_2 \cdots S_{18}$) as a function of the $C_{11}=C_{12}$ dihedral angle. The geometry that was used in the INDO-PSDCI calculation was interpolated between the adiabatic and ground-state conformation by using the above weighting function to interpolate between the Franck-Condon and adiabatic bond lengths, bond angles, and dihedral angles. (As noted above, the C-H bond lengths, the β -ionylidene ring, and a portion of the lysine residue were held fixed.) This approach calculates $S_n \leftarrow S_1$ spectra that approximate those that would be observed via pump-probe techniques as a function of time following absorption of the pump beam by the first excited singlet state. The higher excited-state surfaces are shown in Figure 4. The resulting $S_n \leftarrow S_1$ spectra will be discussed in a separate section to follow.

Origin of the Barrierless Excited-State Surface. The effect of protonation and electronic excitation into the lowest excited $\pi, \pi^* {}^1B_u^+$ state on the atomic charge distributions in the 11-cis, 6-s-cis chromophore of rhodopsin is shown in Figure 3. These charge distributions were calculated for a "vacuum" environment. Local counterions will shift the electron distribution to maximize electrostatic stabilization. In the case of the protonated species, counterion charge redistribution can be significant.³⁴ There are two key observations that can be made. First, the imine nitrogen atoms are negatively charged in both the Schiff base and the protonated Schiff bases. Therefore, models which suggest that a negative counterion is stabilizing a positively charged nitrogen atom are suspect. The positive charge is highly delocalized, the most positively charged atoms being C_{15} , C_{13} , and the imine proton. Second, the protonated Schiff base charge distribution changes dramatically upon excitation, with a net shift of electron density toward the nitrogen atom. For example, the net charge on the $C_{13}=C_{14}-C_{15}=N$ moiety changes from +0.120 to -0.153 upon excitation. Placement of a counterion in this region increases, rather than decreases, the extent of charge reorganization due to polarization of the charge distribution in the ground state and stabilization of conformations which tend to enhance a polarized π -electron system. Thus, the counterion repulses the chromophore in the planar excited state. This charge reorganization is the principal factor in generating a barrierless excited-state potential surface for 11-cis \rightarrow 11-trans photoisomerization.

Dynamics and Quantum Efficiencies of Photoisomerization. The semiempirical molecular dynamics procedures employed in this study are identical to those described in refs 16-18, and the reader is referred to these references for details. As noted above, however, the binding site model employed in these previous studies is incorrect, and thus the ground- and excited-state surfaces in the present study differ from those reported previously. In addition, we explore the potential contribution of nonadiabatic coupling in describing the probability of crossing into the ground state. Nonadiabatic coupling was not included in any of our previous calculations.

(43) Dewar, M. J. S.; Thiel, W. *J. Am. Chem. Soc.* **1977**, *99*, 4899.

(44) Dewar, M. J. S.; Zoebisch, E. G.; Healy, E. F.; Stewart, J. J. P. *J. Am. Chem. Soc.* **1985**, *107*, 3902-3909.

(45) Birge, R. R.; Bocian, D. F.; Hubbard, L. M. *J. Am. Chem. Soc.* **1982**, *104*, 1196.

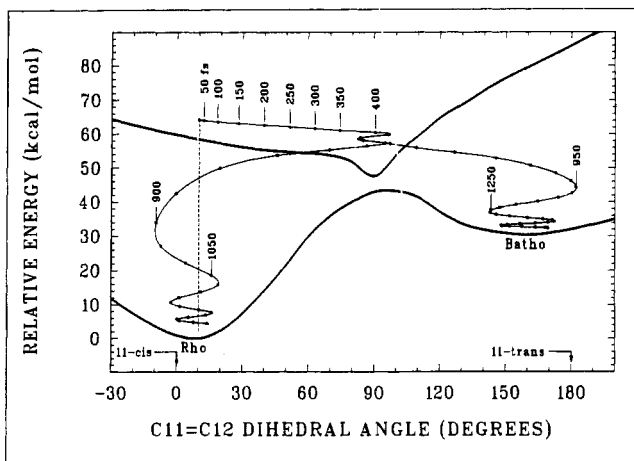


Figure 5. Molecular dynamics of the rhodopsin (Rho) → bathorhodopsin (Batho) photochemical transformation based on the adiabatic ground and first excited singlet state potential energy surfaces shown in Figure 4. The molecule is promoted into the excited state from a rest position with an excess vibrational energy (E_{vib}) of 0.25 eV (5.77 kcal mol⁻¹), and the dynamics of photoisomerization are simulated by solving the classical equations of motion. (Note that the excess vibrational energy includes no torsional kinetic energy, and thus the molecule starts from a rest position in the excited state.) Each dot represents a time interval of 50 fs, and selected time increments relative to the initial excitation are labeled. The excited-state species enters the activated complex (the excited-state potential well with a minimum energy near $\phi_{11-12} = 90^\circ$) in ~ 375 fs and oscillates with an average frequency of torsional motion of 6.59×10^{12} Hz (220 cm⁻¹). Each time the molecule crosses the $E_1 - E_0$ energy minimum at $\phi_{11-12} \approx 90^\circ$, a portion of the excited-state species cross into the ground state and relax to form the isomerized product (bathorhodopsin) or return to the starting configuration (rhodopsin). Two of the early trajectories responsible for repopulating the ground-state surface are shown. Analyses of the ground-state repopulation statistics for various $S_1 \leftrightarrow S_0$ coupling models are shown in Tables I, III, and V.

The probability of crossing into the ground state, $a_0^2(\tau)$, is given by the equation^{16,19,46}

$$a_0^2(\tau) = \left\{ \int_0^\tau \left[\left\langle \psi_1 \left| \frac{\partial \psi_0}{\partial t} \right\rangle a_1(t) \exp \left(\frac{-2\pi i}{h} \int_0^t \Delta E_{10} dt' \right) \right] dt \right\}^2 \quad (3)$$

where ψ_0 and ψ_1 are the electronic wavefunctions of the ground and excited state, respectively, ΔE_{10} is the time-dependent potential energy difference between the excited state and the ground state, and $a_1(t)$ is the population in the excited state at time t . While eq 3 can in principle be evaluated by using numerical methods, the integral involving ΔE_{10} is poorly behaved because it is an oscillating complex function when the integral exceeds \hbar . We have found that eq 3 must be numerically evaluated over very small time regions with constant update of the $a_1(t)$ term to yield reasonable results. While our work on this problem continues, to date we find an unacceptable step-size dependence that precludes accurate implementation with our present computational facilities. In contrast, the semiempirical methods that we have adopted are well-behaved, are computationally tractable, and yield good agreement with experiment.

In our previous studies of rhodopsin photochemistry¹⁶⁻¹⁸ we adopted the semiclassical methods of Miller and George⁴⁶ to calculate the probability of crossing into the ground state. The Miller and George method neglects differential nonadiabatic coupling (see below) and assumes that the probability of crossing is dominated by the dynamic properties of the trajectories

$$a_{\text{dyn}}^2(\tau) = \exp \left\{ \left(\frac{-8\pi \Delta W(\tau)}{3h} \right) \left[\frac{2\Delta W(\tau)}{(\partial^2 \Delta E_{10} / \partial t^2)_{t=\tau}} \right]^{1/2} \right\} \quad (4)$$

(46) Miller, W. H.; George, T. F. *J. Chem. Phys.* **1972**, *56*, 5637-5652.

Table I. Statistical Analysis of the Quantum Yield for Cis → Trans Photoisomerization of Rhodopsin Based on Probabilities of Trajectory Splitting into the Ground State Excluding Nonadiabatic Coupling

pass no. ^a	τ , ps ^b	$a_{\text{dyn}}^2(\tau)$ ^c	S_1 ^d	S_0^{cis} ^e	S_0^{trans} ^f	τ_0^g , ps	τ_0^h , ps
1	0.400	0.345	0.656	0.0	0.345	0.779 (t)	1.253
2	0.473	0.263	0.483	0.172	0.345	0.851 (c)	1.325
3	0.571	0.257	0.359	0.172	0.469	0.949 (t)	1.423
4	0.635	0.305	0.249	0.282	0.469	1.013 (c)	1.487
5	0.723	0.380	0.154	0.282	0.564	1.101 (t)	1.575
6	0.784	0.463	0.083	0.353	0.564	1.162 (c)	1.636
7	0.866	0.463	0.045	0.353	0.602	1.244 (t)	1.718
8	0.929	0.446	0.025	0.373	0.602	1.307 (c)	1.781
9	1.007	0.425	0.014	0.373	0.613	1.385 (t)	1.859
10	1.069	0.411	0.008	0.379	0.613	1.447 (c)	1.921
11	1.145	0.393	0.005	0.379	0.616	1.523 (t)	1.997
12	1.207	0.381	0.003	0.381	0.616	1.585 (c)	2.059
13	1.282	0.366	0.002	0.381	0.617	1.660 (t)	2.134
14	1.343	0.356	0.001	0.382	0.617	1.721 (c)	2.195
15	1.417	0.343	0.000	0.382	0.618	1.795 (t)	2.269
16	1.478	0.333	0.000	0.382	0.618	1.856 (c)	2.330
(1/e)	0.564		0.368	0.172	0.460	0.944 (t)	1.418

^a Trajectory pass through the 90° dihedral angle of the C₁₁₋₁₂ bond. Trajectory passes 3 and 4 are shown in Figure 5. ^b Trajectory time in picoseconds. ^c Probability of crossing into the ground state at τ based on dynamic term. ^d Fraction of molecules remaining in the excited state after trajectory splitting. ^e Fraction of molecules that will equilibrate to form the 11-cis conformation. ^f Fraction of molecules that will equilibrate to form the 11-trans conformation. ^g Total trajectory time until molecule populates the ground state with excess vibrational energy less than 20 kcal/mol or until molecule reaches the edge of the initial trajectory into the ground state, whichever is longer. The resulting geometry is indicated in parentheses (t, 11-trans; c, 11-cis). ^h Total trajectory time for molecule to reach relaxed ground state (see text).

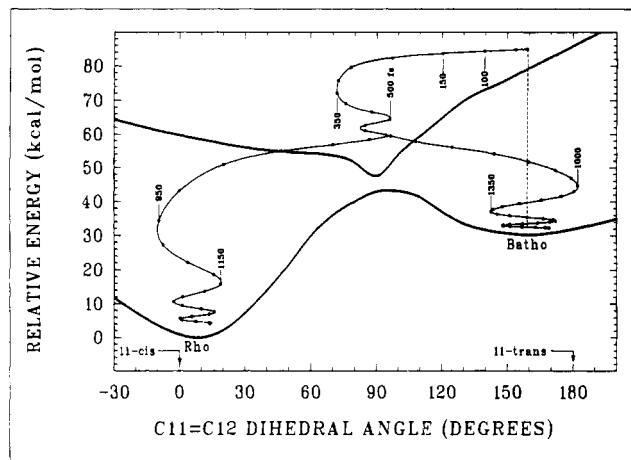


Figure 6. Molecular dynamics of the bathorhodopsin (Batho) → rhodopsin (Rho) photochemical transformation based on the adiabatic ground and first excited singlet state potential energy surfaces shown in Figure 4. The molecule is promoted into the excited state from a rest position with an excess vibrational energy (E_{vib}) of 0.25 eV (5.77 kcal mol⁻¹), and the dynamics of photoisomerization are simulated by solving the classical equations of motion. Each dot represents a time interval of 50 fs, and selected time increments relative to the initial excitation are labeled. The excited-state species enters the activated complex (the excited-state potential well with a minimum energy near $\phi_{11-12} = 90^\circ$) in ~ 210 fs and oscillates with an average frequency of torsional motion of 5.53×10^{12} Hz (185 cm⁻¹). Each time the molecule crosses the $E_1 - E_0$ energy minimum at $\phi_{11-12} \approx 90^\circ$, a portion of the excited-state species cross into the ground state and relax to form the isomerized product (rhodopsin) or returns to the starting configuration (bathorhodopsin). Two of the early trajectories responsible for repopulating the ground-state surface are shown. Analyses of the ground-state repopulation statistics for various $S_1 \leftrightarrow S_0$ coupling models are shown in Tables II, IV, and VI.

where $\Delta W(\tau)$ is the adiabatic potential energy difference between the ground and excited state and the subscript "dyn" refers to dynamic. We modified the Miller and George treatment by

Table II. Statistical Analysis of the Quantum Yield for Trans \rightarrow Cis Photoisomerization of Bathorhodopsin Based on Probabilities of Trajectory Splitting into the Ground State Excluding Nonadiabatic Coupling

pass no. ^a	τ^b , ps	$a_{\text{dyn}}^2(\tau)^c$	S_1^d	$S_0^{\text{cis}}^e$	$S_0^{\text{trans}}^f$	$\tau_{0,8}^g$, ps	$\tau_{0,h}^g$, ps
1	0.213	0.001	0.999	0.001	0.000	0.779 (c)	1.253
2	0.457	0.020	0.979	0.001	0.020	0.835 (t)	1.309
3	0.528	0.031	0.948	0.031	0.020	0.906 (c)	1.380
4	0.622	0.058	0.893	0.031	0.076	1.000 (t)	1.474
5	0.686	0.098	0.805	0.119	0.076	1.064 (c)	1.538
6	0.773	0.170	0.668	0.119	0.213	1.151 (t)	1.625
7	0.833	0.249	0.503	0.285	0.213	1.261 (c)	1.735
8	0.917	0.366	0.319	0.285	0.396	1.295 (t)	1.769
9	0.977	0.439	0.179	0.425	0.396	1.355 (c)	1.829
10	1.055	0.419	0.104	0.425	0.471	1.433 (t)	1.907
11	1.117	0.405	0.062	0.467	0.471	1.495 (c)	1.969
12	1.193	0.388	0.038	0.467	0.495	1.571 (t)	2.045
13	1.254	0.376	0.024	0.481	0.495	1.632 (c)	2.106
14	1.329	0.362	0.015	0.481	0.504	1.707 (t)	2.181
15	1.390	0.351	0.010	0.487	0.504	1.768 (c)	2.242
16	1.464	0.339	0.007	0.487	0.507	1.842 (t)	2.316
(1/e)	0.895		0.368	0.285	0.347	1.300 (c)	1.744

^a Trajectory pass through the 90° dihedral angle of the C₁₁=C₁₂ bond. Trajectory passes 4 and 5 are shown in Figure 6. ^{b-h} As in Table I.

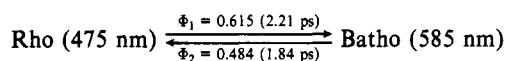
including vibrational relaxation and calculating $\Delta W(\tau)$ by using the formula¹⁶⁻¹⁸

$$\Delta W(\tau) = \Delta E_{10}(\tau) - \Delta E_{10}(\text{lm}) + \frac{1}{4}E_{\text{vib}}(\tau) \quad (5)$$

where $\Delta E_{10}(\text{lm})$ is the difference in the excited-state and ground-state potential energy surfaces at the minimum energy separation (near $\phi_{11,12} = 90^\circ$). The rationale for adopting this procedure has been discussed in detail in our previous papers.¹⁶⁻¹⁸

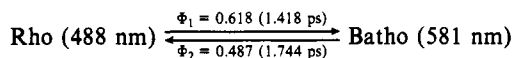
The results of our new simulations of the Rho \rightarrow Batho and Batho \rightarrow Rho photoconversions are presented in Tables I and II and in Figures 5 and 6. The quantum yield calculations shown in Tables I and II are based solely on dynamic coupling (eqs 4 and 5) to provide a perspective on the effect that our revised surfaces have on the calculated quantum yields and kinetics. The results indicate that the revised surfaces yield shorter formation times but generate only a modest increase in the quantum yields for the reactions.

To compare the results shown in Tables I and II with our previous simulations, the key results calculated in refs 16-18 are summarized in Scheme I, where the Rho \rightarrow Batho quantum yield Scheme I

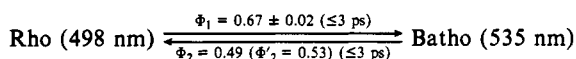


is given by Φ_1 , the Batho \rightarrow Rho quantum yield is given by Φ_2 , and the values listed in parentheses following the quantum yields give the expectation value of the formation of the relaxed ground state corresponding to depopulation of the excited state to 36.8% (1/e). The calculated Franck-Condon absorption maxima are given in parentheses following the Rho (rhodopsin) and Batho (bathorhodopsin) labels. Our new values based on the results given in Figure 4 and Tables I and II are summarized in Scheme II.

Scheme II



As can be seen from a comparison of Schemes I and II, our revised binding site geometry and the resulting surfaces generate faster reaction times but generate only a modest increase in the quantum yields. Experimental values are given in Scheme III, where the Scheme III



λ_{max} assignments are ambient temperature values from Table I of ref 1, the kinetic data are consensus values from refs 11 and 47-52, and the quantum yields are from refs 12-15. The literature

is in general agreement on the value of Φ_1 ,^{12,13} but literature values for Φ_2 range from 0.33¹³ to 0.49.^{14,15} The latter value is more recent, and thus we will use it for comparison. Nevertheless, further experimental investigations to assign Φ_2 would be welcome. Although our revised binding site model provides an improved description of the absorption maxima of Rho and Batho (compare Schemes I-III), we still overestimate the transition energy of rhodopsin by $\sim 400 \text{ cm}^{-1}$ and underestimate the transition energy of bathorhodopsin by $\sim 1500 \text{ cm}^{-1}$. Furthermore, we underestimate the energy storage in bathorhodopsin by $\sim 600 \text{ cm}^{-1}$ ($1.7 \text{ kcal mol}^{-1}$). Given the approximations inherent in our semi-empirical procedures and our neglect of chromophore-protein interactions other than those depicted in Figure 2, we consider this level of agreement with experiment to be satisfactory. Errors in our calculated transition energies will have an impact on the accuracy of the excited-state spectra that are calculated, and this issue will be discussed below.

All of our simulations yield formation times which are significantly shorter than the ~ 3 -ps formation times that are proposed currently in the literature. However, a majority of the measurements were carried out with temporal resolutions on the order of ~ 3 ps, and those that were carried out with temporal resolutions below ~ 1 ps monitored bathorhodopsin formation by using wavelengths above the λ_{max} value of bathorhodopsin. Long-wavelength measurements of bathorhodopsin formation times are expected to predict values longer than those predicted by our simulations because we have not included relaxation of the binding site, but only relaxation of the chromophore, in our assignment of formation time. Note that a "fully relaxed" chromophore in our model will have an absorption maximum of 581 nm, red-shifted by ~ 40 nm from the experimental bathorhodopsin absorption maximum.

The appropriate value of Φ_2 to compare with our calculations requires discussion. Bathorhodopsin photoconverts from both rhodopsin ($\Phi_2 = 0.49 \pm 0.03$) and isorhodopsin (9-cis chromophore) ($\Phi_3 = 0.076 \pm 0.006$).¹⁵ We do not include the 9-trans \rightarrow 9-cis reaction pathway in our analysis, and thus we should compare our calculated value of Φ_2 to the following adjusted (isorhodopsin pathway excluded) value:

$$\Phi_2' = \frac{\Phi_2}{1 - \Phi_3} = \frac{0.49 \pm 0.02}{1 - 0.076 \pm 0.006} = 0.53 \pm 0.03 \quad (6)$$

Thus, both the Φ_1 and Φ_2 quantum yields (Scheme II) are approximately 8% lower than the corresponding observed (Scheme III) values. We now examine the potential contributions of the nonadiabatic coupling term, $\langle \psi_1 | \partial \psi_0 / \partial t \rangle$, on the calculated quantum yields.

Contribution of Nonadiabatic Coupling to Ground-State Repopulation. Weiss and Warshel¹⁹ have proposed that nonadiabatic coupling is the primary contributor to the transfer of molecules from the excited singlet state surface into the ground-state manifold. Their analysis using a pair of orthogonalized Löwdin p_z atomic orbitals yielded $a_{\text{na}}^2(\tau) \approx 0.5$. This value yields excellent agreement with the observed rhodopsin \rightarrow bathorhodopsin quantum yield assuming that this probability is identical on each pass through $\phi_{11,12} = 90^\circ$:

$$\Phi_1 = \frac{1}{2 - a_{\text{na}}^2(\tau)} = \frac{1}{2 - 0.5} = 0.67 \quad (7)$$

There are two features of the Weiss and Warshel model, however,

(47) Green, B.; Monger, T.; Alfano, R.; Anton, B.; Callender, R. H. *Nature (London)* **1977**, *269*, 179-180.

(48) Shichida, Y.; Yoshizawa, T.; Kobayashi, T.; Ohtani, H.; Nagakura, S. *FEBS Lett.* **1977**, *80*, 214-216.

(49) Alfano, R. R.; Yu, W.; Govindjee, R.; Becher, B.; Ebrey, T. G. *Biophys. J.* **1976**, *16*, 541-545.

(50) Buchert, J.; Stefancic, V.; Boukas, A. G.; Alfano, R. R.; Callender, R. H.; Akita, H.; Balogh-Nair, V.; Nakanishi, K.; Pande, J. *Biophys. J.* **1983**, *43*, 279-283.

(51) Doukas, A. G.; Junnarkar, M. R.; Alfano, R. R.; Callender, R. H.; Kokitani, T.; Honig, B. *Proc. Natl. Acad. Sci. U.S.A.* **1984**, *81*, 4790-4794.

(52) Huppert, D.; Rentzepis, P. M.; Klier, D. S. *Photochem. Photobiol.* **1977**, *25*, 193-197.

that deserve further examination. First, if $a_{na}^2(\tau) \approx 0.5$ for all trajectory passes, then we may conclude that $\Phi_2 \approx \Phi_1$, and thus the bathorhodopsin \rightarrow rhodopsin quantum yield calculated by using the Warshel-Weiss model will be significantly overestimated unless bathorhodopsin has an unusually large nondynamic decay mode into the ground state. We consider the latter possibility unlikely given the large excited-state gradient that is calculated for bathorhodopsin. Second, extrapolation of integral calculations based on two orthogonalized Löwdin p_z atomic orbitals to a polyene with six double bonds will likely overestimate the $\langle \psi_1 | \partial \psi_0 / \partial \phi \rangle$ integrals. The above observations notwithstanding, our simulations based on dynamic coupling consistently underestimate the quantum yields. We conclude that nonadiabatic coupling is likely to be an important contributor to $S_1 \leftrightarrow S_0$ coupling. We investigate this issue quantitatively below.

The Miller and George semiclassical model embodied in eq 2 above is based on solution of eq 8 (see eq 3.26 of ref 46), where

$$a_{1-0}(\tau) = \left\langle \psi_1 \left| \frac{\partial \psi_0}{\partial t} \right. \right\rangle_{t=\tau} \left[\frac{h}{2\Delta E_{10}(\tau)} \right]^{1/2} \times \exp \left[-\frac{2\Delta E_{10}(\tau)}{3\hbar} \left\{ \frac{2\Delta E_{10}(\tau)}{(\partial^2 \Delta E_{10} / \partial t^2)_{t=\tau}} \right\}^{1/2} - \frac{i}{\hbar} \int_{t=0}^{\tau} E_1 dt - \frac{i}{\hbar} \int_{\tau}^{\tau'} E_0 dt \right] \quad (8)$$

it is assumed that the exponential prefactor equals unity. This substitution can be justified by comparing eq 8 to the "exact" semiclassical solution and noting that the two are equal only if the prefactor is set to 1.⁴⁶ This approach does not necessarily neglect nonadiabatic coupling but rather assumes that the coupling is constant. Unfortunately, the perturbation approximation adopted by Miller and George to generate eq 8 precludes the direct application of this equation, because the exponential prefactor lacks physical significance (see discussion in ref 46). We have chosen the following perturbation approach to include nonadiabatic coupling.

We define the total coupling between the excited state and the ground state to be given by the function

$$a_{\text{dyn}}^2(\tau) = a_{\text{dyn}}^2(\tau) + a_{\text{na}}^2(\tau)[1 - a_{\text{dyn}}^2(\tau)] \quad (9)$$

where $a_{\text{dyn}}^2(\tau)$ is given by eq 4 and $a_{\text{na}}^2(\tau)$ is given by

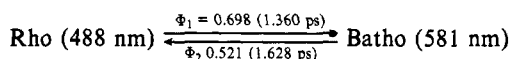
$$a_{\text{na}}^2(\tau) = \left[\left\{ \left(\frac{\partial \phi}{\partial t} \right)_{\text{av}} \right\}^{-1} \int_{\phi_1}^{\phi=90^\circ} \left\langle \psi_1 \left| \frac{\partial \psi_0}{\partial \phi} \right. \right\rangle \left(\frac{\partial \phi}{\partial t} \right)_\phi d\phi \right]^2 \quad (10)$$

where $(\partial \phi / \partial t)$ is the derivative of the $C_{11}=C_{12}$ dihedral angle with respect to time and the integral is carried out from the "start of the trajectory" ($\phi_{11,12} = \phi_1$) to the crossing point ($\phi_{11,12} = 90^\circ$). The derivative $(\partial \phi / \partial t)_{\text{av}}$ is averaged over the interval $\phi_1 - \phi_{11,12} = 90^\circ$. The dihedral angle at the start of the trajectory is equal to the $C_{11}=C_{12}$ dihedral angle upon initial excitation into the excited state $\phi_{11,12} = 8^\circ$, or after a single pass through the crossing region, $\phi_{11,12} = 90^\circ$. Thus, after the first pass, the integration is carried out from $\phi_{11,12} = 90^\circ$ to the turning point and then back to $\phi_{11,12} = 90^\circ$.

Evaluation of $\langle \psi_1 | \partial \psi_0 / \partial \phi \rangle$ is carried out in increments of $\Delta\phi = 0.125^\circ$ or 0.25° by representing the ground-state wave function, ψ_0 , as the highest energy occupied molecular orbital (HOMO) of the closed shell ground state and the excited-state wave function, ψ_1 , as the lowest energy occupied molecular orbital (LUMO). This approximation would be rigorous if the lowest excited singlet state were represented entirely as a LUMO \leftarrow HOMO one-electron excitation. As previously noted,^{17,18,45} however, the lowest excited singlet state has complex configurational character with doubly-excited configurations making major contributions to the configurational character at $C_{11}=C_{12}$ dihedral angles near 90° . Fortunately, two configurations dominate the excited singlet state configurational description: the singly-excited LUMO(α) \leftarrow

HOMO(β) virtual excitation and the doubly-excited spin-coupled LUMO(α)LUMO(β) \leftarrow HOMO(β)HOMO(α) virtual excitation. (The latter is a coupled triplet-triplet transition which spin-couples to form a singlet excited configuration.) Thus, we anticipate that our approach, while not rigorous, will provide a good approximation to $\langle \psi_1 | \partial \psi_0 / \partial \phi \rangle$.

The results for two different orbital phasings are shown in Figures 7 and 8 for $C_{11}=C_{12}$ dihedral angles near 90° . The issue of phasing is critical to an evaluation of the integral that appears in eq 10. The phase of a molecular orbital is not observable, and numerical diagonalization procedures generate arbitrarily phased molecular orbitals. In other words, multiplying all of the eigenvectors by -1 does not affect the eigenvalue or the calculation of any other observable. However, it is essential to adjust the phases of the LUMO and HOMO molecular orbitals prior to carrying out an evaluation of the $\langle \psi_1 | \partial \psi_0 / \partial \phi \rangle$ term to prevent arbitrary sign changes in $\langle \psi_1 | \partial \psi_0 / \partial \phi \rangle$ as a function of ϕ . We did this by monitoring the overlap integrals $\langle \psi_0(\phi) | \psi_0(\phi + \Delta\phi) \rangle$ and $\langle \psi_1(\phi) | \psi_1(\phi + \Delta\phi) \rangle$ and rephasing the $\psi_0(\phi + \Delta\phi)$ and $\psi_1(\phi + \Delta\phi)$ molecular orbitals by multiplying all of the coefficients by -1 if the respective overlap integral is negative. (We note that these procedures are only relevant to situations involving real eigenvectors.) Following these procedures we generate the results shown in Figure 7. The four graphs plot values of $\langle \psi_1 | \partial \psi_0 / \partial \phi \rangle$ (in (a) and (b)) and $[\langle \psi_1 | \partial \psi_0 / \partial \phi \rangle (\partial \phi / \partial t)] / (\partial \phi / \partial t)_{\text{av}}$ (in (c) and (d)) for the two step sizes ($\Delta\phi = 0.125^\circ$ and 0.25°) and indicate that the results are invariant to step size within ~ 2.5 significant digits. The key observation is that the (properly phased) nonadiabatic integrals change sign at $\phi_{11,12} \approx 92^\circ$. If this observation has physical significance, $(a_{\text{na}})^2$ will be significantly larger for the forward (Rho \rightarrow Batho) trajectory than for the reverse (Batho \rightarrow Rho) trajectory through the $\phi_{11,12} = 90^\circ$ crossing point. Thus, the contribution of nonadiabatic coupling to the probability of crossing into the ground state is partitioned into trajectory-dependent contributions which preferentially enhances Φ_1 relative to Φ_2 . The results are shown in Tables III and IV and are summarized in Scheme IV. Note that while both Φ_1 and Φ_2 increase



relative to values calculated on the basis of dynamic coupling alone (Tables I and II; Scheme II), the value of Φ_1 increases 13%, whereas Φ_2 increases 7%. Unfortunately, while Φ_2 is now in excellent agreement with experiment, Φ_1 is now 4% too large. Nevertheless, given the approximations that are inherent in our procedures, we consider the results presented in Tables III and IV based on the inclusion of partitioned nonadiabatic coupling to represent reasonable agreement with experiment.

The observation that nonadiabatic coupling preferentially enhances Φ_1 vs Φ_2 has significant mechanistic implications. To investigate this observation further, we carried out a set of calculations that introduce maximum nonadiabatic coupling. This set differs from the preceding calculations in two respects. First, the phasings of the molecular orbitals are adjusted to always produce positive values of the nonadiabatic coupling integrals. (This approach is identical to simply taking the absolute value of the relevant integrals and ignoring the phases of the molecular orbitals.) Second, the probability of crossing due to nonadiabatic coupling is integrated from trajectory edge to trajectory edge rather than using $\Phi_{11,12} = 90^\circ$ as the integration limit. Justification for the use of absolute valued integrals can be provided by noting that we are calculating nonadiabatic coupling based on adiabatic surface wave functions. Thus, it is possible that the sign change that occurs at $\phi_{11,12} \approx 92^\circ$ is not physically meaningful but is introduced solely due to our use of adiabatic surfaces. Justification for the change in integral limits is based on the observation that the nonadiabatic coupling is strong throughout the $80 < \Phi_{11,12} < 100$ region, and thus transfer into the ground state, while highest at $\phi_{11,12} = 90^\circ$, can nevertheless occur at other dihedral angles. Integration from trajectory edge to trajectory edge takes this possibility into account. The impact of the above two changes

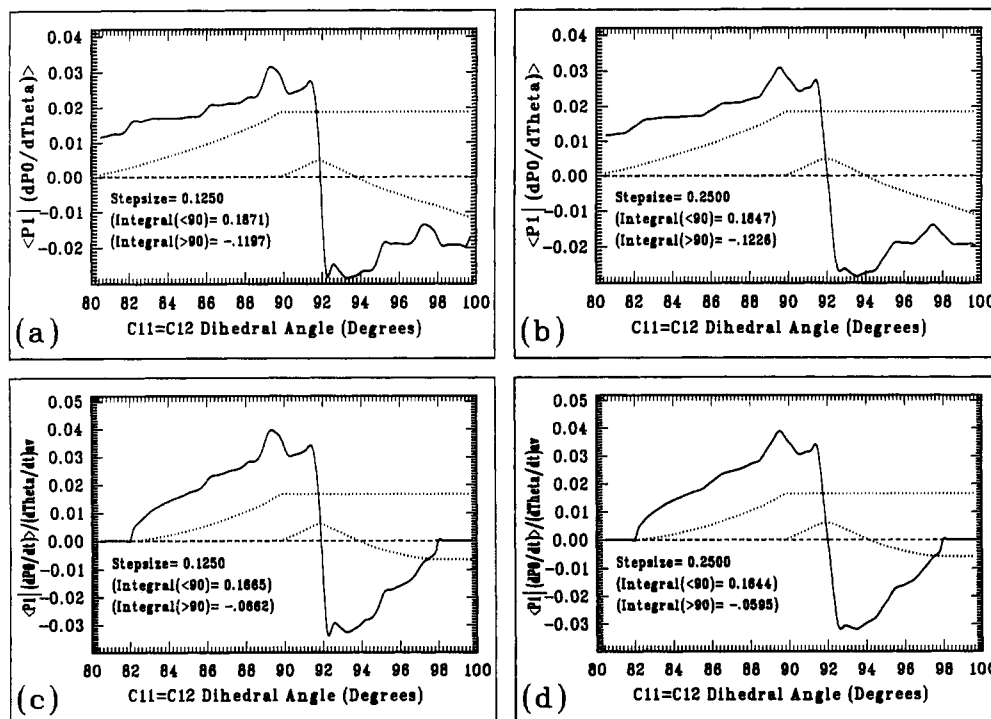


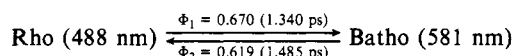
Figure 7. Evaluation of the nonadiabatic coupling terms $\langle \psi_1 | \partial \psi_0 / \partial \phi \rangle$ (top) and $\langle \psi_1 | \partial \psi_0 / \partial t \rangle / (\partial \phi / \partial t)_{av}$ (bottom) calculated in increments of $\Delta \phi = 0.125^\circ$ and 0.25° in the dihedral range $80^\circ < \phi_{11=12} < 100^\circ$. Graphs c and d were calculated for a simulated oscillation of the chromophore within the region $82^\circ < \phi_{11=12} < 98^\circ$, and the $\langle \psi_1 | \partial \psi_0 / \partial t \rangle$ term was calculated by evaluating the product $\langle \psi_1 | \partial \psi_0 / \partial \phi \rangle (\partial \phi / \partial t)$ (see eq 6). The ground-state wave function ψ_0 , is represented as the highest energy occupied molecular orbital (HOMO) of the closed shell ground state, and the excited-state wave function, ψ_1 , is represented as the lowest energy unoccupied molecular orbital (LUMO). The wave functions are phased by monitoring the overlap integrals $\langle \psi_0(\phi) | \psi_0(\phi + \Delta \phi) \rangle$ and $\langle \psi_1(\phi) | \psi_1(\phi + \Delta \phi) \rangle$ and rephasing the $\psi_0(\phi + \Delta \phi)$ and $\psi_1(\phi + \Delta \phi)$ molecular orbitals by multiplying all of the coefficients by -1 if the respective overlap integral is negative. Note that the nonadiabatic integrals change sign at $\phi_{11=12} \approx 92^\circ$. Separate numerical integrations for each graph from $80^\circ < \phi_{11=12} < 90^\circ$ and $90^\circ < \phi_{11=12} < 100^\circ$ are shown by using dotted lines, and the results are tabulated under the stepsize assignment. Thus, $(a_{na})^2$ will be significantly larger for the forward (Rho \rightarrow Batho) trajectory than for the reverse (Batho \rightarrow Rho) trajectory through the $\phi_{11=12} = 90^\circ$ crossing point. Thus, the contribution of nonadiabatic coupling to the probability of crossing into the ground state is partitioned into trajectory direction dependent contributions which preferentially enhances Φ_1 relative to Φ_2 .

Table III. Statistical Analysis of the Quantum Yield for Cis \rightarrow Trans Photoisomerization of Rhodopsin Based on Probabilities of Trajectory Splitting into the Ground State Including Partitioned Nonadiabatic Coupling

pass no. ^a	τ , ^b ps	$a_{na}^2(\tau)$ ^c	$a_{dyn}^2(\tau)$ ^d	S_1^e	$S_0^{cis f}$	$S_0^{trans g}$	τ_0^h , ps	τ_0^i , ps
1	0.400	0.167	0.345	0.546	0.0	0.455	0.779 (t)	1.253
2	0.473	0.026	0.263	0.392	0.154	0.455	0.851 (c)	1.325
3	0.571	0.099	0.257	0.262	0.154	0.584	0.949 (t)	1.423
4	0.635	0.009	0.305	0.181	0.236	0.584	1.013 (c)	1.487
5	0.723	0.072	0.380	0.104	0.236	0.661	1.101 (t)	1.575
6	0.784	0.006	0.463	0.055	0.284	0.661	1.162 (c)	1.636
7	0.866	0.060	0.463	0.028	0.284	0.688	1.244 (t)	1.718
8	0.929	0.005	0.446	0.015	0.297	0.688	1.307 (c)	1.781
9	1.007	0.051	0.425	0.008	0.297	0.695	1.385 (t)	1.859
10	1.069	0.004	0.411	0.005	0.300	0.695	1.447 (c)	1.921
11	1.145	0.044	0.393	0.003	0.300	0.697	1.523 (t)	1.997
12	1.207	0.004	0.381	0.002	0.301	0.697	1.585 (c)	2.059
13	1.282	0.039	0.366	0.001	0.301	0.698	1.660 (t)	2.134
14	1.343	0.004	0.356	0.000	0.302	0.698	1.721 (c)	2.195
(1/e)	0.491			0.368	0.154	0.478	0.886 (t)	1.360

^aTrajectory pass through the 90° dihedral angle of the $C_{11=12}$ bond. Trajectory passes 3 and 4 are shown in Figure 5. ^bTrajectory time in picoseconds. ^cProbability of crossing into the ground state at τ due to nonadiabatic coupling term. ^dProbability of crossing into the ground state at τ due to dynamic term. ^eFraction of molecules remaining in the excited state after trajectory splitting. ^fFraction of molecules that will equilibrate to form the 11-cis conformation. ^gFraction of molecules that will equilibrate to form the 11-trans conformation. ^hTotal trajectory time until molecule populates the ground state with excess vibrational energy less than 20 kcal/mol or until molecule reaches the edge of the initial trajectory into the ground state, whichever is longer. The resulting geometry is indicated in parentheses (t, 11-trans; c, 11-cis). ⁱTotal trajectory time for molecule to reach relaxed ground state (see text).

on the integrals and the resulting photochemistry are examined in Figure 8, Tables V and VI, and Scheme V. The observation Scheme V



that Φ_1 is identical to the experimental value is clearly fortuitous given the observation that Φ_2 is 19% overestimated. We conclude that the sign reversal in the nonadiabatic coupling term shown

in Figure 7 is physically relevant and is in part responsible for Φ_1 being larger than Φ_2 . We conclude further that our simplified treatment of nonadiabatic coupling has merit and indicates that repopulation of the ground state is dominated by dynamic rather than nonadiabatic coupling but that the neglect of nonadiabatic coupling will invariably underestimate the quantum efficiencies associated with rhodopsin and bathorhodopsin photochemistry.

Excited-State Absorption Spectra. The dense manifold of $S_n \leftarrow S_1$ -allowed excited singlet states shown in Figure 4 is responsible

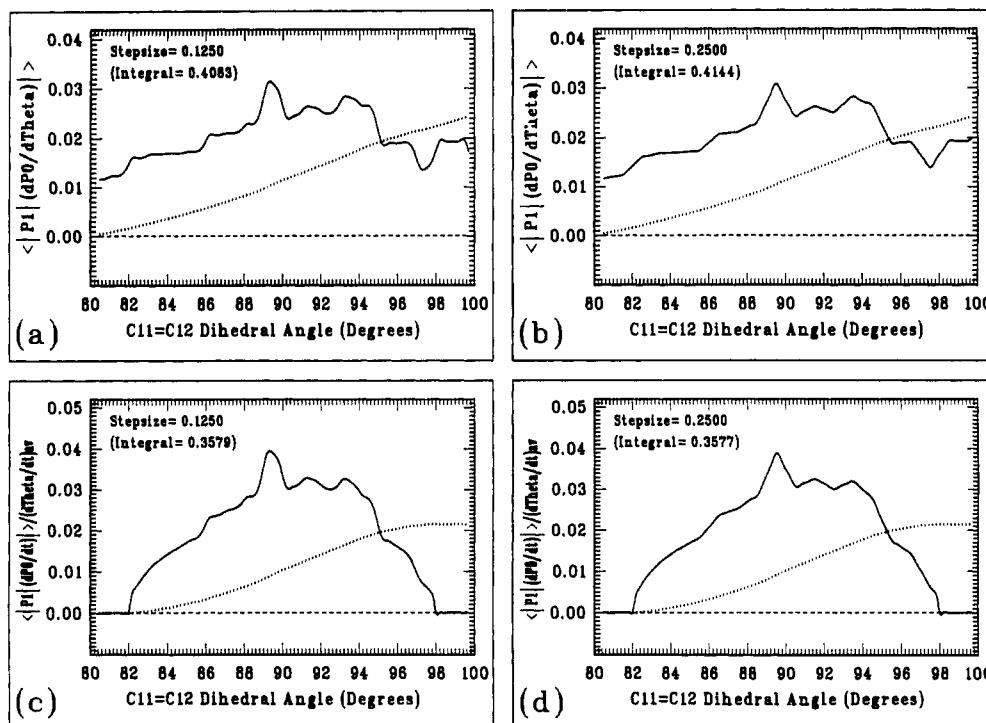


Figure 8. Evaluation of the nonadiabatic coupling terms $\langle \psi_1 | \partial \psi_0 / \partial \phi \rangle$ (top) and $\langle \psi_1 | \partial \psi_0 / \partial t \rangle / (\partial \phi / \partial t)$ (bottom) calculated in increments of $\Delta\phi = 0.125^\circ$ and 0.25° in the dihedral range $80^\circ < \phi_{11=12} < 100^\circ$. Graphs c and d were calculated for a simulated oscillation of the chromophore within the region $82^\circ < \phi_{11=12} < 98^\circ$, and the $\langle \psi_1 | \partial \psi_0 / \partial t \rangle$ term was calculated by evaluating the product $\langle \psi_1 | \partial \psi_0 / \partial \phi \rangle (\partial \phi / \partial t)$ (see eq 6). The ground-state wave function, ψ_0 , is represented as the highest energy occupied molecular orbital (HOMO) of the closed shell ground state, and the excited-state wave function, ψ_1 , is represented as the lowest energy unoccupied molecular orbital (LUMO). Numerical integrations for each graph from $80^\circ < \phi_{11=12} < 100^\circ$ are shown by using dotted lines, and the results are tabulated under the stepsize assignment. Thus, $(a_{na})^2$ will be significantly larger for the forward (Rho \rightarrow Batho) trajectory than for the reverse (Batho \rightarrow Rho) trajectory through the $\phi_{11=12} = 90^\circ$ crossing point. Thus, the contribution of nonadiabatic coupling to the probability of crossing into the ground state is partitioned into trajectory direction dependent contributions which preferentially enhances Φ_1 relative to Φ_2 .

Table IV. Statistical Analysis of the Quantum Yield for Trans \rightarrow Cis Photoisomerization of Bathorhodopsin Based on Probabilities of Trajectory Splitting into the Ground State Including Partitioned Nonadiabatic Coupling

pass no. ^a	τ , ^b ps	$a_{na}^2(\tau)^c$	$a_{dyn}^2(\tau)^d$	S_1^e	S_0^f	$S_0^{trans g}$	τ_0^h , ps	τ_0^i , ps
1	0.213	0.248	0.001	0.751	0.249	0.000	0.779 (c)	1.253
2	0.457	0.147	0.020	0.628	0.249	0.123	0.835 (t)	1.309
3	0.528	0.020	0.031	0.597	0.280	0.123	0.906 (c)	1.380
4	0.622	0.092	0.058	0.510	0.280	0.210	1.000 (t)	1.474
5	0.686	0.008	0.098	0.456	0.334	0.210	1.064 (c)	1.538
6	0.773	0.069	0.170	0.352	0.334	0.313	1.151 (t)	1.625
7	0.833	0.006	0.249	0.264	0.423	0.313	1.261 (c)	1.735
8	0.917	0.056	0.366	0.158	0.423	0.419	1.295 (t)	1.769
9	0.977	0.005	0.439	0.088	0.493	0.419	1.355 (c)	1.829
10	1.055	0.049	0.419	0.049	0.493	0.459	1.433 (t)	1.907
11	1.117	0.004	0.405	0.029	0.513	0.459	1.495 (c)	1.969
12	1.193	0.043	0.388	0.017	0.513	0.471	1.571 (t)	2.045
13	1.254	0.004	0.376	0.011	0.519	0.471	1.632 (c)	2.106
14	1.329	0.038	0.362	0.007	0.519	0.475	1.707 (t)	2.181
15	1.390	0.004	0.351	0.004	0.521	0.475	1.768 (c)	2.242
16	1.464	0.035	0.339	0.003	0.521	0.476	1.842 (t)	2.316
(1/e)	0.760			0.368	0.334	0.297	1.154 (c)	1.628

^a Trajectory pass through the 90° dihedral angle of the $C_{11=12}$ bond. Trajectory passes 3 and 4 are shown in Figure 6. ^{b-i} As in Table III.

for a complex excited singlet state spectrum that can be observed experimentally and should provide insights into the dynamics of rhodopsin photochemistry. Simulations of $S_n \leftarrow S_1$ spectra as a function of trajectory time are shown in Figures 9 and 10. The spectra are simulated by using Gaussian profiles

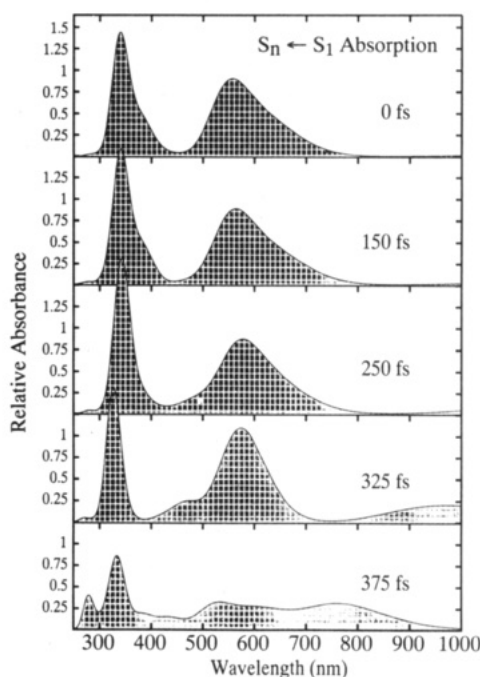
$$A_{rel}(S_n \leftarrow S_1)(\bar{\nu}) = \frac{8\pi^2 m_e c}{3h} \times \sum_{i=2}^n \left\{ \langle S_i | r | S_1 \rangle^2 \exp \left[\frac{-4 \ln(2) (\bar{\nu} - \bar{\nu}_0(S_i) + \bar{\nu}_0(S_1))^2}{\Delta \bar{\nu}^2} \right] \right\} \quad (11)$$

where $A_{rel}(S_n \leftarrow S_1)(\bar{\nu})$ is the relative absorbance at wavenumber $\bar{\nu}$ associated with $S_n \leftarrow S_1$ transitions, $\langle S_i | r | S_1 \rangle$ is the transition

length of the $S_i \leftarrow S_1$ transition, $\bar{\nu}_0(S_i)$ is the energy in wavenumbers of the S_i excited state, $\bar{\nu}_0(S_1)$ is the energy in wavenumbers of the S_1 excited state, $\Delta \bar{\nu}$ is the full-width at half-maximum of the individual Gaussian profiles (assumed identical for all transitions), and the summation is carried out over all n excited states above the first excited singlet state. The present set of calculations included 18 excited singlet states ($n = 18$), and this effectively limits our simulations to spectral regions below 40000 cm^{-1} ($\lambda > 250 \text{ nm}$). We assigned $\Delta \bar{\nu} = 3000 \text{ cm}^{-1}$, a value that has been found to be a good approximation for simulating the one-photon and two-photon spectra of bacteriorhodopsin based on individual electronic transitions (see Figure 5 of ref 53).

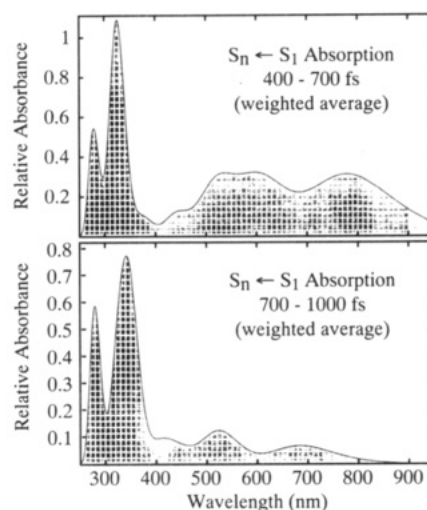
Table V. Statistical Analysis of the Quantum Yield for Cis \rightarrow Trans Photoisomerization of Rhodopsin Based on Probabilities of Trajectory Splitting into the Ground State Including Maximum Nonadiabatic Coupling

pass no. ^a	τ , ^b ps	$a_{na}^2(\tau)$ ^c	$a_{dyn}^2(\tau)$ ^d	S_1 ^e	S_0^{cis} ^f	S_0^{trans} ^g	τ_0^* , ^h ps	τ_0^i , ⁱ ps
1	0.400	0.196	0.345	0.527	0.0	0.473	0.779 (t)	1.253
2	0.473	0.152	0.263	0.329	0.198	0.473	0.851 (c)	1.325
3	0.571	0.114	0.257	0.217	0.198	0.586	0.949 (t)	1.423
4	0.635	0.101	0.305	0.135	0.279	0.586	1.013 (c)	1.487
5	0.723	0.083	0.380	0.078	0.279	0.644	1.101 (t)	1.575
6	0.784	0.077	0.463	0.038	0.318	0.644	1.162 (c)	1.636
7	0.866	0.069	0.463	0.019	0.318	0.663	1.244 (t)	1.718
8	0.929	0.064	0.446	0.010	0.327	0.663	1.307 (c)	1.781
9	1.007	0.058	0.425	0.005	0.327	0.668	1.385 (t)	1.859
10	1.069	0.054	0.411	0.003	0.329	0.668	1.447 (c)	1.921
11	1.145	0.050	0.393	0.002	0.329	0.669	1.523 (t)	1.997
12	1.207	0.047	0.381	0.001	0.330	0.669	1.585 (c)	2.059
13	1.282	0.044	0.366	0.001	0.330	0.670	1.660 (t)	2.134
14	1.343	0.042	0.356	0.000	0.330	0.670	1.721 (c)	2.195
(1/e)	0.439			0.368	0.198	0.434	0.866 (t)	1.340

^{a-i} As in Table III.**Figure 9.** Simulation of $S_n \leftarrow S_1$ absorption of rhodopsin as a function of time following excitation into the first excited singlet state. The spectra are simulated by using oscillator strength weighted Gaussian profiles with all full-width at half-maxima equal to 3000 cm^{-1} . The approximate $C_{11}=C_{12}$ dihedral angles at each time increment are as follows: 0 fs (10.3°); 150 fs (27.8°); 250 fs (51.6°); 325 fs (67.7°); 375 fs (82.1°). The key feature of the early time spectra (0–325 fs) is the presence of a strong absorption centered between 540 and 580 nm, which is surprisingly similar in oscillator strength and energy to the λ_{\max} absorption band of bathorhodopsin. This feature is associated with $S_n \leftarrow S_1$ transitions into excited singlet states S_3 and S_4 shown with dashed lines in Figure 4.

As noted above, our calculated absorption maxima for Rho and Batho differ from the experimental values by 400 ($\Delta\lambda = -10\text{ nm}$) and -1500 cm^{-1} ($\Delta\lambda = 46\text{ nm}$), respectively. Comparable error in the calculated excited-state absorption spectra should be anticipated, and thus the absorption bands shown in Figures 9 and 10 should be compared with experimental values by using the full-widths at half-maxima ($\Delta\tilde{\nu} = 3000\text{ cm}^{-1}$) as approximate error bars.

The spectra shown in Figure 9 are for trajectory times prior to arrival at the activated complex, and the spectra shown in Figure 10 are for trajectory times subsequent to arrival at the activated complex. The key feature of the early time spectra (0–325 fs) is the presence of a strong absorption centered between 540 and 580 nm, which is surprisingly similar in oscillator strength and energy to the λ_{\max} absorption band of bathorhodopsin. This feature

**Figure 10.** Simulation of $S_n \leftarrow S_1$ absorption spectra of rhodopsin as a function of time following excitation into the first excited singlet state subsequent to arrival at the activated complex. The spectra were simulated by using oscillator strength weighted Gaussian profiles with all full-width at half-maxima equal to 3000 cm^{-1} . The top graph shows the spectrum of molecules in the activated complex with an excess vibrational energy of $\sim 0.3\text{ eV}$, whereas the bottom graph shows the spectrum of the molecules in activated complex after the vibrational energy has decayed to $\sim 0.2\text{ eV}$. The simulated spectra are generated in 50-fs increments, and because the molecule spends a majority of its time in the activated complex near the trajectory edges (turning regions), the spectra are dominated by contributions at $\sim 84^\circ$ and $\sim 95^\circ$ (top spectrum) and $\sim 87^\circ$ and $\sim 92^\circ$ (bottom spectrum). Note that while in the activated complex, the molecules are rapidly dropping back into the ground and only $\sim 20\%$ of the molecules remain in the excited state at $\sim 700\text{ fs}$. Thus, while the top spectrum is observable, the bottom spectrum will be difficult if not impossible to observe experimentally.

is associated with $S_n \leftarrow S_1$ transitions into excited singlet states S_3 and S_4 shown with dashed lines in Figure 4. This is an important observation, because this band could be mistaken for an absorption band of ground-state bathorhodopsin. This feature broadens and decreases in intensity once the molecule passes beyond $\phi_{11,12} = 80^\circ$ (375-fs spectrum of Figure 9 and 10). A longer wavelength band at $\sim 780\text{ nm}$ appears after $\sim 375\text{ fs}$, which is diagnostic of $C_{11}=C_{12}$ dihedral angles in the region $80^\circ < \phi_{11,12} < 100^\circ$. All spectra display a strong absorption band at $\sim 340\text{ nm}$, and this band is relatively insensitive in both location and intensity to the $C_{11}=C_{12}$ dihedral angle.

Summary and Conclusions

(1) The ground-state surface connecting rhodopsin and bathorhodopsin along the $\phi_{11,12}$ dihedral angle was adiabatically mapped by using the binding site models shown in Figure 2 and MNDO/AM1 molecular orbital procedures. The steepest descent

Table VI. Statistical Analysis of the Quantum Yield for Trans \rightarrow Cis Photoisomerization of Bathorhodopsin Based on Probabilities of Trajectory Splitting into the Ground State Including Maximum Nonadiabatic Coupling

pass no. ^a	τ , ^b ps	$a_{na}^2(\tau)$ ^c	$a_{dyn}^2(\tau)$ ^d	S_1 ^e	S_0^{cis} ^f	S_0^{trans} ^g	τ_0^* , ^h ps	τ_0^i , ⁱ ps
1	0.213	0.314	0.001	0.685	0.315	0.000	0.779 (c)	1.253
2	0.457	0.171	0.020	0.556	0.315	0.129	0.835 (t)	1.309
3	0.528	0.138	0.031	0.465	0.407	0.129	0.906 (c)	1.380
4	0.622	0.107	0.058	0.391	0.407	0.203	1.000 (t)	1.474
5	0.686	0.095	0.098	0.319	0.479	0.203	1.064 (c)	1.538
6	0.773	0.079	0.170	0.244	0.479	0.278	1.151 (t)	1.625
7	0.833	0.074	0.249	0.170	0.553	0.278	1.261 (c)	1.735
8	0.917	0.064	0.366	0.101	0.553	0.347	1.295 (t)	1.769
9	0.977	0.062	0.439	0.053	0.602	0.347	1.355 (c)	1.829
10	1.055	0.056	0.419	0.029	0.602	0.371	1.433 (t)	1.907
11	1.117	0.053	0.405	0.016	0.613	0.371	1.495 (c)	1.969
12	1.193	0.049	0.388	0.009	0.613	0.378	1.571 (t)	2.045
13	1.254	0.046	0.376	0.006	0.617	0.378	1.632 (c)	2.106
14	1.329	0.043	0.362	0.004	0.617	0.380	1.707 (t)	2.181
15	1.390	0.041	0.351	0.002	0.618	0.380	1.768 (c)	2.242
16	1.464	0.039	0.339	0.001	0.618	0.381	1.842 (t)	2.316
(1/e)	0.643			0.368	0.430	0.203	1.011 (c)	1.485

^{a-i} As in Table IV.

excited-state surface was generated by using a dynamically weighted Franck-Condon and adiabatic surface based on INDO-PSDCI procedures including both single- and double-configuration interaction.

(2) Excitation of rhodopsin into the lowest-lying Franck-Condon excited state generates a large redistribution of the charge resulting in the transfer of ~ 0.27 electron unit of negative charge into the C₁₃...N₁₆ portion of the polyene chain (see Figure 3). This charge reorganization alters the electrostatic interaction with the counterion from a ground-state stabilization into an excited-state destabilization and forces the chromophore away from the counterion. Torsion about the C₁₁=C₁₂ bond is the path of minimum energy, and thus the photoisomerization is initiated with a negative barrier (Figure 4).

(3) Torsion about the C₁₁=C₁₂ bond is calculated to mix the second excited ¹A_g⁻ state into the lowest-lying ¹B_u⁺ state. In the torsional region 75–105° (90° = orthogonal), the lowest excited state has considerable ¹A_g⁻ character. This generates a local minimum in the excited-state potential surface which is referred to as the "activated complex". The activated complex is reached in ~ 375 fs following excitation.

(4) After entering the activated complex, the torsional trajectory is trapped in the dihedral region 80° < $\phi_{11,12}$ < 100° and oscillates with an average frequency of ~ 6.6 oscillations/ps. The first time the excited-state species pass through the orthogonal dihedral region (where the ground- and excited-state species pass through the orthogonal dihedral region (where the ground- and excited-state surfaces come in closest proximity) between 35% and 45% of the molecules transfer into the ground state to form bathorhodopsin. The remaining molecules continue to oscillate within the activated complex, and each time the ensemble passes through $\phi_{11,12} = 90^\circ$, a fraction of the molecules transfers into the ground state. When the molecules are oscillating in the reverse direction [$(\partial\phi/\partial t) < 0$], all molecules transferring into the ground state re-form the starting material, rhodopsin. Conversely, when the excited-state ensemble is oscillating in the forward direction [$(\partial\phi/\partial t) > 0$], all molecules transferring into the ground state form bathorhodopsin.

(5) The quantum yields (Φ) and the product formation times (t) were calculated on the basis of three semiclassical coupling models: (a) purely dynamic coupling (eqs 4 and 5), (b) dynamic and phased (partitioned) nonadiabatic coupling (eqs 4, 5, 9, and 10), and (c) dynamic and absolute (maximized) nonadiabatic coupling. Best agreement with experiment was obtained by using (b) with the results

$$\text{Rho (488 [498] nm)} \xrightarrow[\tau_2 = 0.521 [0.53]; t_2 = 1.628 [3] \text{ ps}]{\tau_1 = 0.698 [0.67]; t_1 = 1.360 [3] \text{ ps}} \text{Batho (581 [535] nm)}$$

where the experimental values are listed in brackets. The forward (Φ_1) quantum yield is overestimated by $\sim 4\%$, and the reverse is

underestimated by 2%. The product formation times are underestimated relative to the literature values (≤ 3 ps), due in part to resolution limitations of the experimental measurements and in part to the fact that the experimental values include protein relaxation that is neglected in our simulations. Note further that the experimental value for Φ_2 is adjusted to remove the isorhodopsin (all-trans \rightarrow 9-cis) pathway. (See Scheme III and subsequent discussion for more detailed examination of these issues.)

(6) The nonadiabatic coupling term, when properly phased, changes sign at $\phi_{11,12} \cong 92^\circ$ (see Figure 7). Thus, coupling into the ground state is enhanced preferentially for the forward (Rho \rightarrow Batho) trajectory relative to the reverse (Batho \rightarrow Rho) trajectory through the $\phi_{11,12} = 90^\circ$ crossing point. Thus, the contribution of nonadiabatic coupling to the probability of crossing into the ground state is partitioned into trajectory-dependent contributions which preferentially enhances Φ_1 relative to Φ_2 . Nonadiabatic coupling also increases the overall efficiency of coupling into the ground state and decreases the product formation time for both the forward and reverse photochemistry.

(7) The lower quantum yield of the bathorhodopsin \rightarrow rhodopsin photoisomerization is due to the above partitioning of the nonadiabatic coupling as well as the rapid arrival of the trajectory into the activated complex. The latter precludes equilibration of the excited state prior to arrival at the activated complex and lowers the dynamic coupling term (compare Tables III and IV).

(8) The dense manifold of $S_n \leftarrow S_1$ -allowed excited singlet states shown in Figure 4 is responsible for a complex excited singlet state spectrum which displays a time dependence (Figures 9 and 10). The key feature of the early time spectra (0–325 fs) is the presence of a strong absorption centered between 540 and 580 nm, which is surprisingly similar in oscillator strength and energy to the λ_{\max} absorption band of bathorhodopsin. This band could be mistaken for an absorption band of ground-state bathorhodopsin. This feature broadens and decreases in intensity once the molecule passes beyond $\phi_{11,12} = 80^\circ$ (375-fs spectrum of Figures 9 and 10). A longer wavelength band at ~ 780 nm appears after ~ 375 fs, which is diagnostic of C₁₁=C₁₂ dihedral angles in the region 80° < $\phi_{11,12}$ < 100°. All spectra display a strong absorption band at ~ 340 nm, and this band is relatively insensitive in both location and intensity to the C₁₁=C₁₂ dihedral angle.

Acknowledgment. This work was supported in part by a grant to R.R.B. from the National Institutes of Health (GM-34548). The computer facilities in the Center for Molecular Electronics were provided by grants from Digital Equipment Corp. and the W. M. Keck Foundation. Additional computer facilities were provided by the Northeast Parallel Architecture Center at Syracuse University. We thank Drs. R., H. Callender, B. Honig, A. F. Lawrence, R. A. Mathies, T. P. Sakmar, A. Warshel, and R. M. Weiss for interesting and helpful discussions.